Title: Low variability runoff inhibits coupling of climate, tectonics, and topography in the Greater Caucasus

---

This manuscript has been submitted for publication in *Earth and Planetary Science Letters*. This version has been revised in response to peer review, but is still currently under review and subsequent versions of this manuscript may have slightly different content. If accepted, the final version of this manuscript will be accessible via the "Peer-reviewed Publication DOI" link on the right-hand side of this webpage. Please feel free to contact the authors, we welcome feedback.

Author and Affiliations:
Adam M. Forte[1], Joel S. Leonard[2], Matthew W. Rossi[3], Kelin X. Whipple[2], Arjun M. Heimsath[2], Lasha Sukhishvili[4], Tea Godoladze[4], Fakhraddin Kadirov[5]

[1]Department of Geology & Geophysics, Louisiana State University, Baton Rouge, LA, USA
[2]School of Earth and Space Exploration, Arizona State University, Tempe, AZ, USA
[3]Earth Lab, Cooperative Institute for Research in Environmental Sciences (CIRES), University of Colorado, Boulder, CO, USA
[4]Institute of Earth Sciences and National Seismic Monitoring Center, Ilia State University, Tbilisi, Georgia
[5]Institute of Geology and Geophysics of Azerbaijan National Academy of Sciences, Baku, Azerbaijan

Corresponding Author: Adam M. Forte (aforte8@lsu.edu)
ORCID ID: 0000-0003-4515-7792
Twitter Handle: @AdamForte83

Low variability runoff inhibits coupling of climate, tectonics, and topography in the Greater Caucasus

Adam M. Forte[1], Joel S. Leonard[2], Matthew W. Rossi[3], Kelin X. Whipple[2], Arjun M. Heimsath[2], Lasha Sukhishvili[4], Tea Godoladze[4], Fakhraddin Kadirov[5]

[1]Department of Geology & Geophysics, Louisiana State University, Baton Rouge, LA, USA
[2]School of Earth and Space Exploration, Arizona State University, Tempe, AZ, USA
[3]Earth Lab, Cooperative Institute for Research in Environmental Sciences (CIRES), University of Colorado, Boulder, CO, USA
[4]Institute of Earth Sciences and National Seismic Monitoring Center, Ilia State University, Tbilisi, Georgia
[5]Institute of Geology and Geophysics of Azerbaijan National Academy of Sciences, Baku, Azerbaijan

Corresponding Author: Adam M. Forte (aforte8@lsu.edu)

Highlights

- Large, new cosmogenic dataset from the Greater Caucasus
- Channel steepness index sublinearly varies with erosion rates
- Stochastic-threshold incision model explains erosion-steepness relationship
- Nonlinearity interpreted to reflect orographic controls on snowmelt runoff
- Precipitation phase may modulate degree of climate-tectonic coupling possible

Abstract

Hypothesized feedbacks between climate and tectonics are mediated by the relationship between topography and long-term erosion rates. While many studies show monotonic relationships between channel steepness and erosion rates, the degree of nonlinearity in this relationship varies by landscape. Mechanistically explaining controls on this relationship in natural settings is critical because highly nonlinear relationships imply low sensitivity between climate and tectonics. To this end, we present a carefully coordinated analysis of cosmogenic ^{10}Be concentrations in river sands paired with topographic, hydroclimatic, and tectonic data for the Greater Caucasus Mountains where topography is invariant along-strike despite large gradients in modern precipitation and convergence rates. We show that spatial patterns in erosion rates largely reflect regional tectonics with little sensitivity to mean precipitation or runoff. The nonlinearity in the erosion rate – steepness relationship arises from very low runoff variability which we attribute to the large contribution from snowmelt. Transitioning from

rainfall- to snowmelt-driven runoff as mean elevation increases is common to many mid-latitude mountain ranges. The associated decrease in runoff variability may represent important, unrecognized dynamics inhibiting the sensitivity of tectonics to climate more broadly.

1. Motivation

The potential for dynamic coupling between climate and tectonics has driven decades of research. However, empirical data are equivocal with results both supporting and rejecting such coupling (Whipple, 2009). The extent to which climate can influence tectonics in fluvial landscapes depends both on the sensitivity of topography to climatic variables (e.g., precipitation, runoff) and tectonic ones (e.g., convergence, uplift) (Willett, 1999). If the response of topography to increasing uplift and erosion rates is sublinear, then large changes in rates can only drive slight changes in fluvial relief and the potential for two-way coupling is low (Whipple and Meade, 2004). In this study, we focus on daily runoff variability, which when paired with a threshold to incision, strongly influences the form of the topography-erosion rate relationship (e.g., DiBiase and Whipple, 2011; Lague, 2014; Lague et al., 2005). Under this view, regions with extremely low runoff variability should exhibit a highly nonlinear topography-erosion rate relationship. We examine this expectation in the Greater Caucasus (GC), where prior work demonstrates a lack of simple climatic or tectonic influences on topography despite substantial along-strike gradients in both (Forte et al., 2016). We present a large, new suite of basin-averaged ^{10}Be erosion rates along with detailed analyses of topography, tectonics, and hydroclimate to evaluate whether very low runoff variability in the GC attributed to snowmelt hydrology can explain the apparent disconnect between climate, tectonics, and topography. We then consider results in the broader context of how the relative contributions from snowmelt versus rainfall runoff are expected to change as mountain ranges grow.

2. Background

2.1 Fluvial Incision Modeling

The rate of bedrock erosion by rivers, E [L/t], is often estimated using the stream power incision model (Lague, 2014) (SPIM):

$$E = KA^m S^n \quad (1)$$

where K [L^{1-2m}/t] is a constant encapsulating climate and substrate properties, A [L^2] is drainage area as a proxy for discharge, S [L/L] is local river slope, and m and n are dimensionless constants related to erosional process, friction relationship, and width scaling (Lague, 2014). Within this framework, it is useful to consider a normalized metric of channel steepness that accounts for the expected co-variation of drainage area and slope. Normalized channel steepness index (k_{sn} [$L^{2m/n}$]) is an empirical relationship (e.g., Kirby and Whipple, 2012) of the form:

$$k_{sn} = A^{\theta_{ref}} S \quad (2)$$

where θ_{ref} is a dimensionless index describing the concavity of a channel. In the context of SPIM, θ_{ref} is equivalent to m/n at steady state. Substituting eq. 2 into eq. 1 generates a direct, if simple, prediction relating long term erosion rates, E, to the topography of a landscape as described by k_{sn} (Kirby and Whipple, 2012; Lague, 2014):

$$k_{sn} = K^{-1/n} E^{1/n} \quad (3)$$

At steady state, n governs the sensitivity of topography to changes in tectonics or climate whereby high values imply weaker coupling (e.g., Whipple and Meade, 2004). Globally, E-k_{sn} relationships vary widely and range from linear to highly sublinear (Harel et al., 2016; Kirby and Whipple, 2012; Lague, 2014), necessitating consideration of this relationship at the landscape scale when evaluating potential climate-tectonic coupling.

While predictions from SPIM explain a variety of observations (Kirby and Whipple, 2012), its simplicity impedes interpretation of the shape of E-k_{sn} relationships. One promising alternative are models that incorporate event-scale runoff variability with erosion thresholds, i.e. stochastic threshold incision models (STIM) (Campforts et al., 2020; Deal et al., 2018; DiBiase and Whipple, 2011; Lague et al., 2005; Scherler et al., 2017; Tucker, 2004) where the instantaneous incision rate I is expressed as:

$$I = K\bar{R}^m Q^{*\gamma} S^n - \Psi_c \tag{4}$$

$\bar{R}$ [L/t] is mean discharge ($\bar{Q}$ [L^3/t]) divided by drainage area, $Q^*$is daily discharge divided by mean daily discharge, γ is the local discharge exponent, and Ψ_c is a threshold parameter that scales with the critical shear stress for incision (τ_c [$LM^{-1}T^{-2}$]) and substrate erodibility (k_e [$L^{2.5}T^2M^{-1.5}$]). Eq. 4 reduces to eq. 1 for a constant runoff ($Q^* = 1$) and zero threshold (Ψ_c=0). Under STIM, the long-term erosion rate, *E*, is the integration of eq. 4 over a distribution of discharges:

$$E = \int_{Q_c(k_s)}^{Q_m} I(Q, k_s) pdf(Q) dQ \tag{5}$$

where Q_c is the minimum discharge that exceeds τ_c, $Q_m$is the maximum discharge considered, and the $pdf(Q)$ is the probability distribution of discharge. While a variety of probability distributions have been used (e.g., Lague et al., 2005; Tucker, 2004)(e.g., Tucker, 2004; Lague et al., 2005), we use here a two parameter Weibull distribution:

$$pdf(Q^*; Q_0, c) = \frac{c}{Q_0}\left(\frac{Q^*}{Q_0}\right)^{c-1} e^{-(Q^*/Q_0)^c} \tag{6}$$

where c is a variability parameter describing the shape of the distribution and Q_0 is a scale parameter related to the mean of the distribution. Weibull distributions have been shown to describe a wide array of observed daily discharge distributions (Rossi et al., 2016) and better characterize observations in the GC than the more commonly used inverse gamma distribution (Lague, 2014). Application and derivation of the general form of STIM is well documented and thus we refer interested readers to prior studies (e.g., Campforts et al., 2020; Deal et al., 2018; DiBiase and Whipple, 2011; Lague, 2014; Lague et al., 2005; Scherler et al., 2017; Tucker, 2004).

The conceptual framing for STIM (Lague et al., 2005; Tucker, 2004) was built around rainfall events that trigger runoff over the span of hours to days. Stochastic descriptions of streamflow can be similarly built for snowmelt processes, which are potentially important in our study area, as long as they account for the transient accumulation and release of snow water (Schaefli et al., 2013). While there have been efforts to integrate snowmelt hydrology into the STIM framework (Deal et al., 2018), we fully recognize that the complex dynamics of long duration, snowmelt hydrographs on sediment entrainment, deposition, and bedrock erosion (e.g., Johnson et al., 2010) is not well represented by the probability distribution of flows alone. Nevertheless, accounting of the probability distribution of flows is a necessary, if not sufficient, step towards building an erosion law that can account for both rainfall and snowmelt runoff. By using STIM as a unifying framework, the degree of nonlinearity of the E-k_{sn} relationship is directly related to watershed hydrology via the variability parameter (Deal et al., 2018). Settings with lower discharge variability and thus higher values of c will exhibit more nonlinear E-k_{sn} relationships, all other things being equal.

2.2 Regional Setting

The Greater Caucasus Mountains (GC) represent the northernmost extent of deformation caused by the Arabia-Eurasia collision. In the central portion of this collision, the GC are the main locus of shortening since plate reorganization at ~5 Ma (Allen et al., 2004). While the timing of reorganization coincides with rapid exhumation throughout the GC (e.g., Avdeev and Niemi, 2011; Vincent et al., 2020), large uncertainties remain as to the location, rates, and nature of major structures within the GC (e.g., Cowgill et al., 2016). Since ~1-2 Ma, active shortening largely stepped out from the range and localized on a series of foreland fold-thrust belts along its northern and southern flanks. However, uplift is kinematically linked to active shortening via the geometry of active faults at depth within the main range (e.g., Forte et al., 2014, 2013; Mosar et al., 2010; Trexler et al., 2020). Modern convergence (Reilinger et al., 2006) and precipitation (Forte et al., 2016) rates vary by an order-of-magnitude along strike, with shortening increasing and precipitation decreasing eastward (Fig. 1). While along-strike patterns in convergence are complex (Fig. S1), we focus on the component accommodated along the southern range front where we collected new samples (Fig. 1). Whether modern geodetic velocities represent long-term convergence rates remains controversial (Forte et al., 2016), though geodetic rates of shortening are at least consistent with average rates of shortening from the last 1-2 Ma estimated from balanced cross-sections (Forte et al., 2013; Trexler et al., 2020).

Theory suggests that along-strike variations in precipitation and convergence rates should lead to an eastward increase in mean elevation and local relief (Whipple and Meade, 2004). This is not observed in the GC and is not explained by potential confounding factors like glaciation and lithological heterogeneity (Forte et al., 2016). Instead, topography is relatively invariant along-strike with an across-strike pattern of lower relief flanks and a higher relief core (Forte et al., 2016) (Fig. 1). Prior studies attributed the across-strike gradient in topography to a northward increase in uplift rates along the southern flank of the GC with local maxima near drainage divides (Forte et al., 2015). Forte et al. (2016) also evaluated whether trends in mean precipitation were masking other important climate gradients (e.g., streamflow variability) that might better explain topographic patterns, to no avail. They concluded that invariant topography along-strike was either due to a: (1) disconnect between modern tectonics and climate with the longer-term forcing, or (2) complex, co-varying relationships between the two. However, interpreting topography alone is fraught, and testing such hypotheses requires careful sampling of erosion rate data (e.g., DiBiase et al., 2010; Scherler et al., 2014), a key motivation for this study.

Prior estimates of exhumation and erosion rates in the GC largely come from low-temperature thermochronology (e.g., Avdeev and Niemi, 2011; Vincent et al., 2020, 2011) and modern sediment yields and provenance (e.g., Vezzoli et al., 2020). Thermochronology data, mostly concentrated west of 44°E, suggests older cooling ages along the lower relief flanks than the higher relief core, patterns that are broadly reflected in the topography (Forte et al., 2016). Exhumation rates are representative of the last ~5-10 Ma and suggest rates of ~1000 m Myr^{-1} in the core that decrease to <250 m Myr^{-1} towards the flanks (Avdeev and Niemi, 2011; Vincent et al., 2020). Over the modern era, erosion rates inferred from sediment yields and heavy mineral provenance imply similar average rates and spatial patterns, but with erosion rates near the range core >2000-3000 m Myr^{-1} locally (Vezzoli et al., 2020). At the millennial scale, there is only one published basin-averaged, ^{10}Be erosion rate from the Inguri river in the western GC. The 1100 m Myr^{-1} rate (Vincent et al., 2011) is comparable to the long-term and short-term rates, though it averages across significant variations in steepness and major knickpoints, and is thus hard to relate to topography. Our new dataset seeks to fill this knowledge gap by reporting a large, new, millennial-scale, ^{10}Be erosion rate dataset that systematically samples across gradients in topographic relief and hydroclimate in the GC.

3. Methods

To understand how well topography reflects erosion rates, we sampled and measured cosmogenic ^{10}Be in quartz river sands (e.g., Bierman and Nichols, 2004) from 34 carefully selected, locally equilibrated, unglaciated basins (Fig. 1). Sampling was coordinated with analyses of modern tectonics, topography, and hydrology of rivers to better assess predictions of SPIM and STIM fluvial erosion laws. Below, we summarize these methods. Where appropriate, we provide additional detail in the Supplement, and raw data and algorithms are archived in a GitHub repository.

3.1. Characterizing climate, tectonics, and topography

3.1.1 Modern Precipitation and Streamflow

We use rainfall data from the Tropical Rainfall Measurement Mission (TRMM) 3B42 product, and we use basin-averaged standard deviation of mean monthly snow cover calculated from MODIS MOD10C2. The latter dataset is used as a proxy for snowmelt, whereby high values imply significant variation in snow cover through the year (i.e., large amount of snowmelt) and low values imply small variations in snow cover through the year. Data processing of both are described elsewhere (Forte et al., 2016). Daily records of discharge (converted to runoff by dividing by drainage area) for the Caucasus region comes from the Global Runoff Data Centre (GRDC) and was also originally presented elsewhere (Forte et al., 2016). We reprocess runoff data here to remove basins whose variability may be artificially low due to dams and fit the distribution of discharge more carefully, the procedure for which we describe in detail below.

To better understand patterns in daily runoff variability, we sought to partition daily flows into annual, seasonal, and event components (Table S1). Baseflow separation techniques have received much attention (see review by Eckhardt, 2008), and our methods are akin to the widely used 'sliding interval' baseflow separation method of Sloto & Crouse (1996). However, baseflow separation efforts typically focus on binary separation of the overland flow component of the hydrograph. Given our somewhat different objectives, we instead seek to decompose hydrographs into three components: (1) an event component that includes event-scale overland flow and subsurface contributions, (2) a seasonal component that includes the lagged release of snowmelt runoff and autocorrelated series of rainstorms, and (3) slower inter-annual changes to the water table. To this end, we quantify the inter-annual component using the 365-day moving minima and the seasonal component using a 31-day moving minima minus the annual component. The event-driven component is inferred from the daily flows minus both the seasonal and annual components, thus satisfying the condition that the three components sum to the total streamflow (Fig. S2). While drainage area differences will influence the temporal lag of runoff responses to rainfall or snowmelt inputs, our analysis focuses only on the regularity of flows under uniform intervals. In much the same way that our estimates of mean runoff and runoff variability implicitly subsume the role of drainage area, so does our partitioning of the time series of streamflow. To develop a climatology of daily flows, we also calculated mean daily runoff as a function of day of year and apply a 31-day moving mean to smooth over the influence of individual, large events. Similar analyses on mean daily rainfall from TRMM are only used to determine the timing and magnitude of peak rainfall in the main text, though full time series are shown in Fig. S3.

3.1.2 Modern convergence rates

To compare erosion rates to modern convergence rates, we follow prior efforts which divided GPS velocities into either a Greater Caucasus or Lesser Caucasus domain (Avdeev and Niemi, 2011; Forte et al., 2014) and calculated average velocities along-strike using a sliding 50-km moving window (Fig. S1). Convergence between the Lesser and Greater Caucasus is the difference between these velocities along-strike. Our results are similar to prior estimates (Forte et al., 2014), but incorporate updated GPS velocities (Sokhadze et al., 2018).

3.1.3 Topographic metrics

Topographic analyses of individual basins used TopoToolbox (Schwanghart and Scherler, 2014) and TAK for TopoToolbox (Forte and Whipple, 2019). Specifically, we relied on 'ProcessRiverBasins' and related tools within TAK to calculate basin-averaged statistics of topography and climatology. For basin-averaged topographic metrics, we use the SRTM 30-m DEM and calculated k_{sn} using a reference concavity of 0.5. While this reference concavity is appropriate for the GC (e.g., Forte et al., 2016), we tested whether the observed shape of the relationship between k_{sn} and ^{10}Be erosion rate was sensitive to the choice of reference concavity and found no measurable differences across a range of concavities from 0.3-0.6 (Fig. S4).

3.2. Cosmogenic Erosion Rates from Alluvial ^{10}Be Inventories

Prior to field sampling, we vetted basins that appear to be in local topographic steady-state (i.e., lacking major knickpoints; outside the influence of LGM glaciation) so that basin-averaged, ^{10}Be erosion rates can be reliably related to k_{sn} (Fig. S5). This motivated the sampling of 76 basins across the southern range front of the Greater Caucasus. A subset of 47 were processed for erosion rates (Table S2). Low abundance of quartz and difficulty in processing due to lithology (see discussion in Supplement) resulted in usable amounts of quartz for 34 samples. For each sample, we selected the 0.25-1 mm size fraction and used a combination of traditional HF and HNO_3 leaches and the 'hot phosphoric acid' technique (Mifsud et al., 2013) to isolate and purify quartz. Samples were spiked with either commercial or custom low-background ^{9}Be carrier, Be was extracted through liquid chromatography, and BeO was analyzed by accelerator mass spectrometry at PRIME Lab, Purdue University. To convert blank-corrected, ^{10}Be concentrations into erosion rates, we calculated effective latitude and elevations to determine basin-averaged ^{10}Be production rates (Portenga and Bierman, 2011) and calculated erosion rates in v3.0 of the online calculator formerly known as the CRONUS calculator (Balco et al., 2008). Erosion rates are reported for a time independent scaling scheme (Stone, 2000). Additional details on site selection, sample processing, and erosion rate calculations are provided in the Supplement. All relevant parameters needed to reproduce erosion rates are provided in Table S3.

Due to low quartz yields, we also carefully examined the bedrock geology for each basin (Forte, 2021) to assess the influence of variable quartz sourcing. By recalculating topographic metrics and erosion rates after removing portions of basins with lithologies unlikely to provide quartz, we found no meaningful difference in the E-k_{sn} patterns (Fig. S6, Table S3). As another test on the potential sensitivity to non-uniform quartz yields, we also considered the end-member scenarios where we assume that quartz is entirely sourced from the upper or lower 50% of each basin and recalculated topographic metrics and erosion rates (Fig. S6, Tables S3). We found negligible differences in E-k_{sn} patterns - the central conclusions of this work are insensitive to this complication. For all three cases, recalculated E generally lies within the uncertainty bounds of E calculated assuming equal sourcing from the entire catchment. This suggests that analytical uncertainty on erosion rates encompasses uncertainty in quartz sourcing in this setting.

3.3 Numerical Modeling of River Incision

3.3.1 Parameterization of SPIM

To assess which SPIM parameters best characterize the relationship between channel steepness and ^{10}Be erosion rates, we fit eq. 3 to measured E and k_{sn} data. To do this, we linearize eq. 3 using a log-transform and fit the data using the orthogonal distance regression (ODR) algorithm in SciPy. To estimate ranges of acceptable fits, we tested both a Monte Carlo (similar to Adams et al., 2020) and a bootstrap method. While results are comparable, the bootstrap approach produced wider estimates of uncertainty. As such, we report fits and uncertainties using the bootstrap method as more conservative estimates. In fitting the data, we excluded data from one basin whose uncertainty exceeds its mean value (Fig. S7). We also tested the sensitivity of fits to the two highest erosion rates. While removal of these two rates suggest a lower n, the range of uncertainties inclusive and exclusive of these data substantially overlap (Fig. S7). Given the lack of any meaningful reason to exclude these data, the reported fits include these two high erosion rate basins.

3.3.2 Parameterization of STIM

STIM is a more complex model than SPIM and requires calibration of a larger number of parameters. Prior studies provide more detailed discussion of the derivation of STIM and reasonable parameter values (Campforts et al., 2020; Deal et al., 2018; DiBiase and Whipple, 2011; Lague et al., 2005; Scherler et al., 2017). For this work, parameter values are summarized in the Supplement and many (k_t, ω_a, ω_s, α, β, a) are set to previously used values (e.g., DiBiase and Whipple, 2011). The six parameters we vary and/or explicitly test in our analysis are; $\bar{R}$, c, Q_0, k_w, τ_c, and k_e, each of which are described and justified below.

Because none of the ^{10}Be basins are gauged, we generalize runoff parameters in gauged GRDC basins for attribution. To estimate $\bar{R}$ in sampled basins, we needed to relate $\bar{R}$ (known for gauged basins) with mean precipitation as measured by TRMM ($\bar{P}_{\mathrm{TRMM}}$) (known for all basins). To do this, we fit a power law relationship between $\bar{P}_{\mathrm{TRMM}}$ and $\bar{R}$ in gauged basins (Fig. 2A) and used this relationship to interpolate $\bar{R}$ for ^{10}Be basins (Fig. 2B). It is important to note that this regression implies runoff ratios > 1 for basins with high runoff. We suspect that runoff ratios > 1 are due to the well-known underestimation of snowfall from TRMM (Wulf et al., 2016). Increased snow fraction is generally expected to increase average runoff ratios (e.g., Berghuijs et al., 2014), and the high runoff ratios for basins with high mean runoff are suggestive of an increasing contribution from snowmelt. However, we cannot quantitatively assess how snow fraction may covary with mean precipitation given the uncertainty on $\bar{P}_{\mathrm{TRMM}}$.

Runoff distributions for gauged basins are characterized using the shape (c) and scale (Q_0) parameters of the Weibull distribution (eq. 6). In detail, runoff distributions within the Caucasus are complex and likely represent distinct seasonal components described by different probability distributions (e.g., Scherler et al., 2017). However, unlike prior attempts to account for this using hybrid distributions, the seasonality of the Caucasus is more variable spatially and temporally than monsoonal settings (e.g., Sutcliffe et al., 2008) and thus systematic separation of just two components is untenable. As such, we instead fit a single distribution to each individual gauged record that minimizes the misfit between: (1) the observed $\bar{R}$ and implied $\bar{R}$ of the distribution fit and (2) the shape of the tail of the observed and fit distribution. To do this, we first fit exceedance probability distributions on the ln-linearized right tail of the distribution above a given threshold (Wilson and Toumi, 2005). By varying this threshold from 1% (rare) to 60% (frequent) daily exceedances, we found the threshold that minimizes an objective function that weights a normalized sum of the mean square of the error on the right tail fit and a normalized difference between the observed and implied $\bar{R}$ (Fig. S8). We found the best results when we weighted the difference between the implied and observed mean by 1.5x. Comparing the observed and implied mean $\bar{R}$ (Fig. 3C) and the observed and implied runoff for a flow with a 2-year return interval (as a proxy for how well the tail of the distribution is honored; Fig. 3D) suggests acceptable this method is providing a decent description of both mean and tail statistics.

The scaling between channel width and discharge (k_w) is an important, and hard to constrain, hydraulic geometry relationship that strongly influences the shape of the *E*-k_{sn} relationship predicted by STIM (Lague, 2014). Channel width (w) is typically related to discharge (Q) using the function:

$$w = k_w Q^{\omega_a} \tag{7}$$

where ω_a is a constant we set to 0.5. Following DiBiase and Whipple (2011), we set the value of k_w to 15 but test its importance by comparing observed channel widths to predicted widths for both the mean and 2-year flows (Figs. 4, S10). We measure channel widths for 26 of the 34 sampled basins using satellite imagery and ChanGeom (Fisher et al., 2013). We were unable to measure channel widths for all basins because of poor imagery and/or density of tree cover. This analysis suggests that a k_w of 15 largely encompasses observations and effectively represents a minimum value for k_w. Higher values of k_w imply increasingly nonlinear *E*-k_{sn} relationships. As such, setting this parameter to 15 for all basins ensures that we are not overestimating the degree of nonlinearity based on potential variations in k_w (Fig. 4).

Both the erosional efficiency (k_e) and threshold shear stress (τ_c) control the magnitude of the threshold parameter (Ψ_c) in STIM (eq. 5), neither of which is well constrained for our setting. Given the need to fix one parameter to calibrate the other, our goal is to find a single, best-fit value of k_e that can be used as representative of the entire erosion rate dataset. As an initial step, we first seek to find meaningful divisions within the estimated runoff distributions using k-means clustering on the values of c and $\bar{R}$ from the gauged basins (Figure 5A). Clustering results suggest there are 4 semi-distinct hydroclimatic populations within the gauged basins (Fig. 5A, S11). For each population, we characterize the aggregate $\bar{R}$, c, and Q_0 in two different ways, either by arithmetic means or by creating composite discharge records within each cluster and refitting the composite distribution (for c and Q_0 only). The results of both are similar and we use the refit composite values of c and Q_0 for subsequent components. We then assess which runoff cluster ungauged basins belong to based on estimated $\bar{R}$, the maximum elevation of the catchments (which is correlated with the shape and scale parameters, e.g., Fig. 5C), and geographic proximity to gauged basins (Fig. 5D-E). Within a given cluster, we then fix the distribution parameters c and Q_0 to the aggregate values for that cluster, use the estimated $\bar{R}$ for individual ungauged basins, fix τ_c at 45 Pa, and use STIM to find the $k_e$for each basin that most closely reproduces measured *E* using the known value of k_{sn} (Fig. 6A). To account for uncertainty in both k_{sn} and *E* for each basin, we generate a synthetic distribution of 500 k_{sn} and *E* values using the mean and uncertainties of individual basin values of k_{sn} and *E*. We then find a population of k_e values for each basin such that individual random k_{sn} values drawn from the synthetic k_{sn} distribution minimize the misfit between individual random *E* values drawn from the synthetic *E* distribution. This produces a distribution of k_e values for each ^{10}Be basin. We use the median k_e as our best estimate of k_e for a particular basin and the statistics of this distribution (i.e., interquartile range) as an estimate for uncertainty on this value. To represent populations of basins (whole dataset and clusters), we report medians of best fit k_e values (Fig. 6A). We also do a similar exercise where we fix k_e to the median value from above and estimating τ_c values for individual ^{10}Be basins (Fig. 6B).

The approach we take to estimate k_e (or τ_c) assumes limited influence of lithology on k_e or τ_c, which is consistent with prior results from the GC (Forte et al., 2016, 2014) and reinforced by the lack of correlation between the optimized k_e values and lithology (Fig. S12). While some studies applying STIM to cosmogenic erosion rates use grain size measurement to constrain τ_c (DiBiase and Whipple, 2011), the challenge of obtaining such data prompts many studies like ours to assume a reasonable grain size and corresponding τ_c (Campforts et al., 2020; Scherler et al., 2017), as we do here.

4. Results

4.1 Relating Erosion Rates to Topography

Erosion rates, *E*, vary from 33-5610 m Myr^{-1} (Figs. 7). Rates do not simply vary with along-strike position (Fig. S13), but increase monotonically with LC-GC convergence rates (Forte et al., 2014; Kadirov et al., 2012; Reilinger et al., 2006; Sokhadze et al., 2018) (Fig. 7). Across-strike *E* systematically increases from the southern flanks of the range towards the core, reaching a peak south of the topographic crest (Fig. 7C). Despite the wide range of *E*, all data lie on a single, highly nonlinear relationship between k_{sn} and *E* (Fig. 8A). Similar relationships exist between *E* and mean basin slope due to the quasi-linear relationship between k_{sn} and slope in this setting (Fig. 8C). Remarkably, over erosion rates from ~300 to >5000 m Myr^{-1}, channel steepness is essentially invariant, ranging between ~300-500 m (Fig. 8). While there is substantial scatter in these high *E* and k_{sn} basins, this is not unusual for these kinds of datasets and reflects both geologic and analytical uncertainty in the erosion rate estimates and the merging of two distinct ksn-E relationships associated with catchments in clusters 2 and 3 (30 of 34 data points, Fig. 8A). Moreover, detailed interrogation of potential confounding factors reveals no meaningful way to subdivide these data into different physically interpretable populations (Fig. S14).

4.2 River Incision Modeling

Fitting data with the SPIM (eq. 3) suggests an *n* of 3.1 to 4 with a median value of 3.5 (Fig. 8, Fig. S7). This is in the range of *n* found elsewhere, but well above the global mean value of ~2.5 (Harel et al., 2016; Lague, 2014). *E* does not systemically vary with $\bar{P}_{TRMM}$ (Fig. 8B) or $\bar{R}$ (Fig. 8A). Given this outcome, we turn to STIM which explicitly accounts for daily runoff variability, to see how well it explains the strong nonlinearity in the empirical E-k_{sn} relationship.

Figure 6 shows that optimized k_e varies over six orders of magnitude, though most data lies within 1 order of magnitude of the median k_e (Fig. 6). There is an apparent relation between position within the range and/or erosion rate (which are correlated, e.g., Fig. 7C) and k_e or τ_c (Fig. 6). We further consider possible implications of spatial variations in k_e or τ_c implied from our optimization in the discussion.

Within a given cluster, application of STIM using the whole population k_e and τ_c parameters and either the aggregate or individual gauged basins values of c and Q_0 produces moderate correspondence with the observed E-k_{sn} relationship within that cluster (Fig. 9). Ultimately, while the single SPIM relationship provides a suitable fit to the entire dataset (Fig. 8), the application of the STIM within clusters highlights that the degree of scatter in the observed E-k_{sn} may reflect the detailed hydroclimatic variations within the Caucasus region, facilitating a data-driven interpretation to the nonlinear relationships observed. In detail, the appearance of a pseudo-maximum k_{sn}, appears to largely result from the mixing of primarily two different, but both sublinear E-k_{sn} relationships (i.e., cluster 2 & 3, Fig. 8A).

5. Discussion

5.1 Tectonic Implications for the Greater Caucasus

Our new cosmogenic erosion rates in the GC are broadly consistent with prior million-year and decadal rates. All suggest systematic increases in E toward the core of the range, with maximum E greater than 1000-2000 m Myr^{-1} (Avdeev and Niemi, 2011; Vezzoli et al., 2020; Vincent et al., 2020, 2011), though our maximum rates of ~5000 m Myr^{-1} exceed most estimates from thermochronology or sediment yields. The broad agreement between E and GC-LC convergence rates suggest that millennial scale E faithfully records modern tectonic forcing (Fig. 7). While the degree to which modern GPS velocities (Kadirov et al., 2012; Reilinger et al., 2006; Sokhadze et al., 2018) reflect geologic rates remains controversial (Forte et al., 2016), they are representative of average geologic rates of shortening over the last 1-2 Ma as estimated from balanced cross sections (Forte et al., 2013; Trexler et al., 2020). Spatial patterns in cosmogenic E

are consistent with the expected vertical components of GC-LC shortening rates applied to north-dipping structures with reasonable dips (Fig. 7D), though we emphasize that the geometry of structures in the interior of the GC are not well constrained (e.g., Cowgill et al., 2016; Forte et al., 2014). The across-strike pattern of increasing *E* toward the topographic crest, is consistent with prior suggestions of a thrust ramp beneath the southeastern range-front (e.g., Forte et al., 2015), but does not require this geometry. While there is substantial scatter in these spatial relationships, likely due to local structural complexity, this result strongly contrasts with the poor correlation between *E* and mean rainfall or estimated runoff (Fig. 8). From this, we reject a simple climatic control on *E* in this setting, and the rest of our discussion focuses on what more careful consideration of hydroclimate reveals.

5.2 Application of STIM to the Greater Caucasus

The ability of STIM to reproduce observed E-k_{sn} relationships (Fig. 9) suggests that the shape of this relationship in the GC is aided by considering the systematic decrease in runoff variability with elevation (e.g., Fig. 5C). STIM unpacks the bulk treatment of climate in SPIM by characterizing hydroclimate using a simplified model of runoff generation ($Q = R * A$) and an assumed probability distribution of daily runoff (Weibull parameters c and Q_0, which are genetically related to the empirical mean). The k-means cluster analysis suggests at least four distinct hydroclimatic regimes in the Caucasus (Fig. 5, S11). Specifically, we find clusters generally correspond to high runoff and higher variability (Cluster 1: $\bar{R}$ > 4, c < 1), high runoff and lower variability (Cluster 1: $\bar{R}$ > 4, c > 1), low runoff and higher variability (Cluster 2: $\bar{R}$ < 4, c < 0.9), and low runoff and lower variability (Cluster 3: $\bar{R}$ < 4, c > 0.9). These clusters also have clear spatial relationships, with a general trend of basins with higher maximum elevations corresponding to lower daily runoff variability (Fig. 5C).

Cluster analysis allows us to evaluate model performance in terms of broad variations in hydroclimate. In general, model parameters derived from gauged basins improves E-k_{sn} predictions for ungauged basins (Fig. 9). This is especially true for Cluster 2, which includes the bulk of the erosion rate basins, but also performs acceptably for Cluster 3, despite the apparent mismatch between the imposed k_e and the ranges of k_e for Cluster 3 basins (Fig. 6). The high runoff clusters 1 and 4 do not perform as well with only 1 of the 4 basins being well explained by the model. Given that none of the other 3 basins are clear outliers in the overall E-k_{sn} relationship (Fig. 8A) or relationships between E and convergence velocity (Fig. 7D), we interpret the mismatch to be due to anomalously high k_{sn} in these basins. Lithological differences do not explain these anomalously steep basins (e.g., Fig. S15) indicating that other model parameters must differ for these basins and/or vary systematically with runoff. It is important to note here that the boundaries between clusters appear gradational (Fig. 5C). Thus, the extent to which individual basins are not well explained by predicted E-k_{sn} relationships could in part reflect either (1) incorrect cluster membership or (2) that the true range of discharge distributions are not represented by the admittedly small number of gauged basins.

The observed mismatches within clusters could also reflect real variability in k_e, which we impose as a constant. Optimization of k_e results suggest that rock erodibility increases (or incision thresholds decrease) towards the center of the range (Fig. 6). If real, it could imply a systematic weakening of rocks (or decrease in mean grain sizes) toward the core of the orogen. This could be indicative of more fractured rocks due to periglacial processes or accumulated tectonic damage. There also exists a weak positive correlation between optimized k_e and erosion rate (Fig. 6), which is cross correlated with distance from the center of the range (Fig. 7C). Systematic variations of incision thresholds with increasing erosion rate have been suggested (Shobe et al., 2018), but are thought to operate in the opposite direction whereby more rapid uplift leads to coarser material and less erodible channels. However, the apparent variability within k_e may also be an artifact of discrete clustering of data that reflect a continuum of behavior. For example, clusters 2 and 3 overlap. Use of cluster 2 parameters for cluster 3 largely erases cross-correlations among optimized k_e, erosion rate, and proximity to the core of the range, begging caution in interpreting these findings. Interpretation of these patterns requires detailed observations of rock properties and grain size distribution to provide an additional constraint. Regardless of the challenge of determining which set of parameters are ‘most representative,’ the utility of the cluster analysis is that it highlights that the range of scatter observed in the E-k_{sn} relationship should be expected for the range of hydroclimatic variability observed in this setting. Furthermore, sub-dividing by these hydroclimatic domains reveal that (1) runoff distributions are all strongly sublinear and (2) the sublinear nature of the observed E-k_{sn} relationship in aggregate reflects mixing of a suite of different sublinear relationships, which is dominated by contributions from cluster 2 and 3 (Fig. 8A, 9).

To further probe the E-k_{sn} relationship, we attempt to relate the clusters to their underlying hydroclimatology. Figure 10A shows smoothed mean daily runoffs as a function of time of year. In general, we interpret the strong seasonal signals in the GC as indicative of a dominant component of snowmelt runoff, especially when maxima occur in the spring or summer, though this could reflect other sources (e.g., where seasonal rainfall is correlated with seasonal streamflow). This is consistent with a prior observations in the GC highlighting the importance of spring and summer snowmelt in the hydrology of the range (e.g., Kuchment et al., 2010; Rets et al., 2018; Verdiev, 2009). Snowmelt contributions contribute up to 50% of the runoff during the summer months in high elevation catchments (e.g., Vasil'chuk et al., 2016). For high mean runoffs, both cluster 1 and 4 basins show a strong seasonal signal that is systematically offset from peak precipitation. While cluster 4 generally has a single high runoff mode in the GC, cluster 1 appears more complex with multi-modal seasonality. At lower mean runoff, cluster 2 basins exhibit muted to non-existent seasonality in runoff and less systematic relations to the timing of peak rainfall. Cluster 3 basins show clear seasonality with a dominant peak in runoff in the late spring and early summer. This peak in runoff occurs shortly after a peak in rainfall, also in the late spring, but there is a noticeable peak in the late fall with no corresponding runoff peak which we attribute to the building of a snowpack (Fig. S3). Regardless of cluster, higher elevation basins typically show summer seasonality, reinforcing our interpretation that snowmelt is the dominant driver of seasonal flows throughout the Caucasus region (Fig. 10A).

Figure 10A does not fully characterize the regularity of flows because data were smoothed to develop a seasonal climatology. To probe whether and how well streamflow seasonality explains the runoff variability parameter, c, we also partitioned time series data into three components: event, seasonal, and annual fractions which together sum to the total water flux. For gauged basins, the seasonal component shows a positive correlation with runoff variability (shape), especially for basins in the GC (Fig. 10B). Similarly, the shape and scale parameters exhibit a strong negative correlation with the event component (Fig. S16). Given that we attribute the seasonal component to spring/summer snowmelt with modest contributions from seasonal rainfall in some basins, we interpret patterns in runoff variability to be principally driven by the contribution of snowmelt to runoff. This is reinforced with the observed positive relationship between daily runoff variability (shape) and basin-averaged standard deviation of mean monthly snow cover, a metric used by Forte et al., (2016) as a proxy for snowmelt (Fig. 10C). We thus interpret our STIM results to at least partially account for orographic patterns in runoff variability that embed the long hydrologic response times associated with snowmelt runoff (Deal et al., 2018).

5.3 Implications for Interactions Among Climate, Tectonics, and Topography

The nonlinearity of the E-k_{sn} relationship in the GC explains why prior work (Forte et al., 2016) failed to recognize the influence of either precipitation or convergence gradients in the topography of the range (e.g., Fig. 1). Such a relationship predicts relatively invariant k_{sn} at high erosion rates. Millennial scale erosion patterns are also concordant with convergence rates and proximity to the core of the range (Fig. 7). Higher rates near the core of the range are similar to patterns observed in both sediment flux estimates (Vezzoli et al., 2020, 2014) and bedrock thermochronology (Avdeev and Niemi, 2011; Vincent et al., 2020), suggesting this reflects a fundamental detail of the orogen's architecture. The similar width of the range along-strike (Forte et al., 2014) (Fig. 1) and the low sensitivity of channel steepness to E exceeding 300-500 m Myr^{-1} (Fig. 8A) explains why topography (e.g., mean elevation and local relief) is relatively invariant along-strike. STIM helps reconcile apparently large contrasts in mean annual precipitation and runoff between basins (Fig. 8B) by only considering the role of flows above the incision threshold. While we recognize that the simplistic representation of events in STIM does not fully capture seasonal dynamics in the GC (e.g., Fig. 9,10, S3,S9), the general result that low variability runoff leads to highly nonlinear E-k_{sn} relationships (DiBiase and Whipple, 2011; Lague, 2014; Lague et al., 2005) coupled with the mixing of primarily two different, but both sublinear E-k_{sn} relationships provides a satisfying explanation for the pseudo-threshold-k_{sn} behavior (e.g., Fig. 8, 9) and the lack of a clear climate signal in the topography.

We interpret orographic patterns in variability and the nonlinearity of the E-k_{sn} relationship to the importance of snowmelt. This is consistent with previous work probing seasonal patterns of runoff in the GC (e.g., Kuchment et al., 2010; Rets et al., 2018; Vasil'chuk et al., 2016; Verdiev, 2009) and the more general observation that mountain regions with a large snow fraction tend to have lower event-scale runoff variability (e.g., Rossi et al., 2016) as the dominant flood generating mechanism changes from rainfall to snowmelt runoff (e.g., Berghuijs et al., 2016). Our hypothesized link between the nonlinearity in the E-k_{sn} relation and low variability snowmelt runoff has interesting implications. Under modern climate, only tributary basins on the low elevation and low erosion rate flanks of the range should be topographically sensitive to either climatic or tectonic changes. These areas: (1) have higher runoff variability due to a lesser influence of snowmelt (Fig. 5, 10), and (2) are in the quasi-linear portion of the E-k_{sn} relationship (Fig. 8). Conventional approaches toward accounting for orographic precipitation in landscape evolution have focused on elevation-dependent mean annual rainfall (Bookhagen and Burbank, 2006) or snowfall (Anders et al., 2008). This work highlights the critical role of the transition from rainfall- to snowmelt- driven hydrology in mediating runoff variability itself (Rossi et al., 2020), an important complexity rarely considered in landscape evolution studies. Transitioning from rainfall- to snowmelt-driven hydrology is dictated by the elevation distribution within a mountain range and presents a possible direct relation between climate and erosion rates in orogenic systems, albeit not in the traditional sense where there is a positive correlation between erosion and precipitation or runoff rates (Ferrier et al., 2013) . Importantly, a snowmelt control on runoff variability may be relevant to many mountain ranges where the growth of topographic relief has undermined the erosive ability of higher mean annual precipitation by distributing flows over longer duration snowmelt events.

6. Conclusions

We present a large suite of new basin-averaged ^{10}Be erosion rates from the Greater Caucasus that are consistent with longer term exhumation and shorter-term decadal scale rates. Erosion systematically varies with convergence rates between the Greater Caucasus and Lesser Caucasus and is uncorrelated to mean annual rainfall, favoring a tectonic control on erosion rates. The relationship between erosion and channel steepness is extremely nonlinear in this setting. However, careful consideration of regional hydro-climatology incorporated into a stochastic threshold incision model of river incision reveals that low variability, snowmelt runoff is driving this nonlinearity, thus explaining why prior efforts failed to recognize a clear climatic imprint on topography in the mountain range.

Our results also highlight the importance of both: (1) considering regionally constrained relationships between topography and erosion when assessing potential climate-tectonic interactions, and (2) understanding the underlying mechanism(s) setting that form. In the Greater Caucasus, significant climate-tectonic interactions are precluded because topography becomes insensitive to changes in forcing at uplift rates exceeding 300-500 m Myr^{-1}. This contrasts with settings where relationships between erosion and topography may be more linear. We emphasize that the observed nonlinearity between erosion rates and channel steepness in the GC is not a global solution to an apparent lack of coupling between climate and tectonics. Rather, the wide range of such relationships around the world likely reflects important landscape specific, hydro-climatic details that must be considered when applying erosion models. Our results also show that spatial and temporal patterns in precipitation phase that alter flood frequency may be an underappreciated governor on the degree of climate-tectonic coupling possible in mid-latitude mountain ranges not heavily influenced by glacial erosion.

Acknowledgements

This work was supported by the National Science Foundation grant EAR-1450970 to A.M.F. and K.X.W. We thank Charles Trexler and Alexander Tye for collecting a small subset of the samples used in this analysis; Eric Cowgill and Nathan Niemi for help and advice related to this project both in and out of the field; Dachi Injia, Giga Ugrekhelidze, Davit Kapanadze, and Zurab Javakhishvili for assistance in the field; and Byron Adams and Roman DiBiase for helpful discussions and sharing codes. We acknowledge the

GRDC for providing runoff data, available here (https://www.bafg.de/GRDC/EN/Home/homepage_node.html). We thank Dirk Scherler for comments which improved this manuscript. We also acknowledge the existence of two anonymous reviewers of an earlier draft of this manuscript.

Data Availability

The authors certify that all data necessary to reproduce the key findings of this paper are presented in the manuscript or its supplement. We additionally provide the majority of the data tables as plain text, shapefiles of the ^{10}Be basins, the GRDC basins, some select rasters that are generally not easily available, and many of the analysis scripts in a GitHub repository (https://github.com/amforte/Caucasus_Erosion DOI: 10.5281/zenodo.5752531). The lithologic compilations are provided as a separate open access permanent repository (Forte, 2021: https://doi.org/10.5281/zenodo.5752511).

Figures

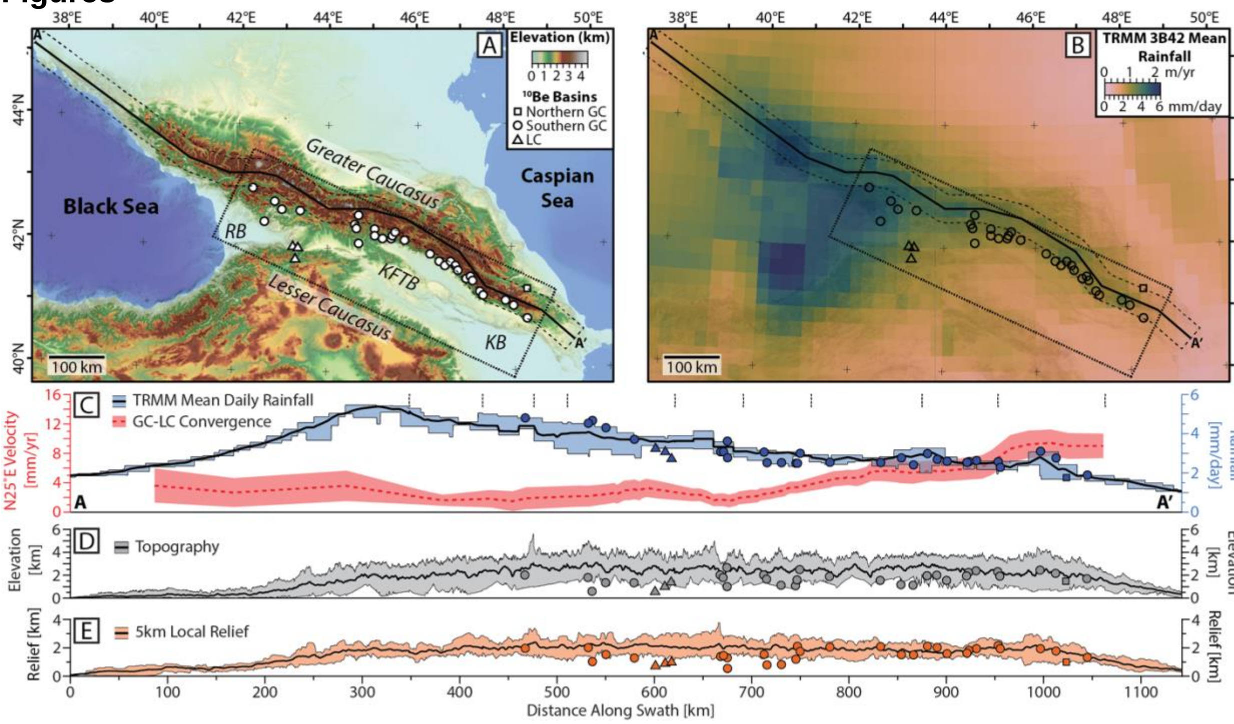

Fig 1. (A) Regional map with location of alluvial cosmogenic ^{10}Be samples (white symbols) within the Greater and Lesser Caucasus (LC). Line A-A' and corresponding box outline 50-km wide swath referenced in other figures and is centered on the topographic crest of the range. Dotted rectangle is outline of Fig 2A. KFTB – Kura Fold Thrust Belt, KB – Kura Basin, RB – Rioni Basin. (B) TRMM 3B42 mean daily rainfall (Forte et al., 2016). (C) Blue shaded region is maximum and minimum rainfall within the swath in panel B (line is mean value). Blue symbols are mean rainfall in sampled basins. Red shaded region is estimated convergence rates between the Greater and Lesser Caucasus along the southern margin of the Greater Caucasus, and id largely similar to that calculated by Forte et al., (2014). It was recalculated to include more recent GPS data (see Supplement and Fig. S1). (D) Swath of topography. Symbols are mean elevation within sampled basins. (E) Swath of local relief using a 5-km radius circular moving window. Symbols are mean relief within sampled basins.

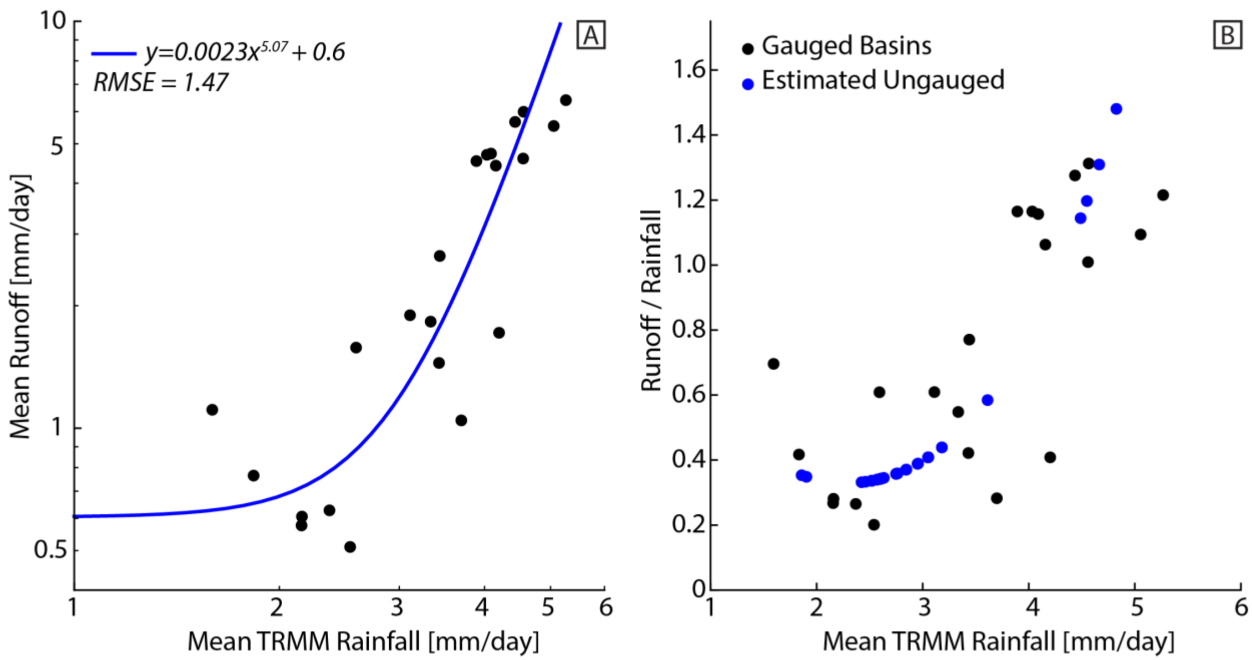

Fig 2. (A) Relationship between mean TRMM rainfall within gauged GRDC basins and mean runoff used to estimate runoff in ungauged basins from mean TRMM rainfall. (B) Comparison between mean TRMM rainfall and implied runoff ratio for both the gauged basins and the ungauged basins. Note that both in the gauged and ungauged basins, runoff ratios exceed 1 at high rainfall (runoff) rates. This likely implies an underestimation of TRMM rainfall, e.g., from missing snowfall (Wulf et al., 2016), as opposed to a real runoff ratio which exceeds 1.

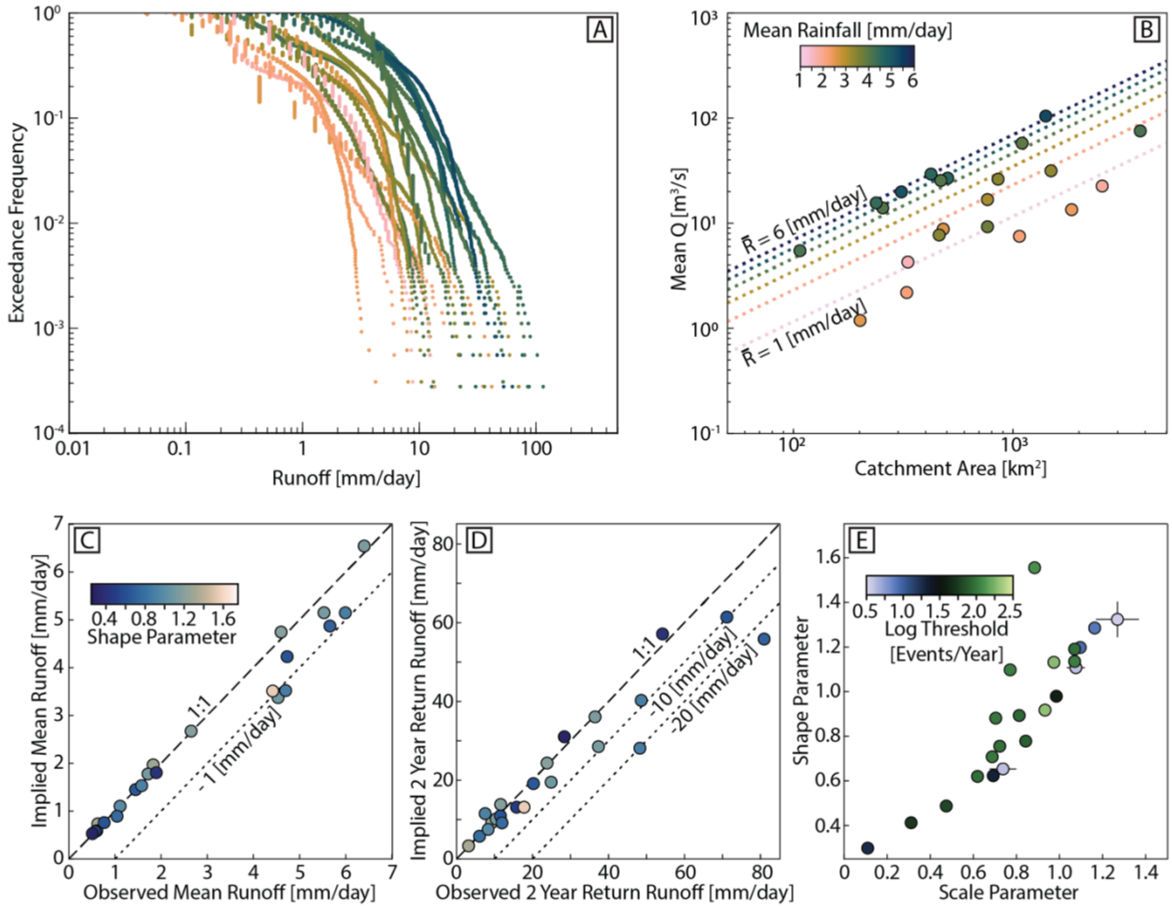

Fig 3. (A) Exceedance frequency versus daily runoff for each GRDC basin and colored by mean rainfall estimated from TRMM 3B42. Runoff calculations assume a linear scaling with drainage area, see 2B. (B) Mean discharge versus drainage area colored by mean rainfall for each GRDC basin. The quasi-linear relationship between discharge and drainage area, after parsing by mean rainfall, is consistent with a linear scaling of runoff ($\bar{Q} = \bar{R}A$). Lines represent constant mean runoff assuming this linear scaling. (C) Comparison of observed mean runoff and that implied by the fitting of the individual gauged basin discharge distributions with a Weibull (stretched exponential) distribution, see text for details. (D) Comparison of observed and implied 2 year return flood runoff magnitudes from the fitting of the distributions. (E) Comparison of shape and scale parameters resultant from the fits. Dots are scaled by the threshold (i.e., average number of events per year that define the tail of the distribution) that yielded the best fit for individual basins. Fig. S8 provides an example of the fitting technique we use and Fig. S9 compares the results of our preferred fitting technique and a fit of the whole distribution via the method of moments.

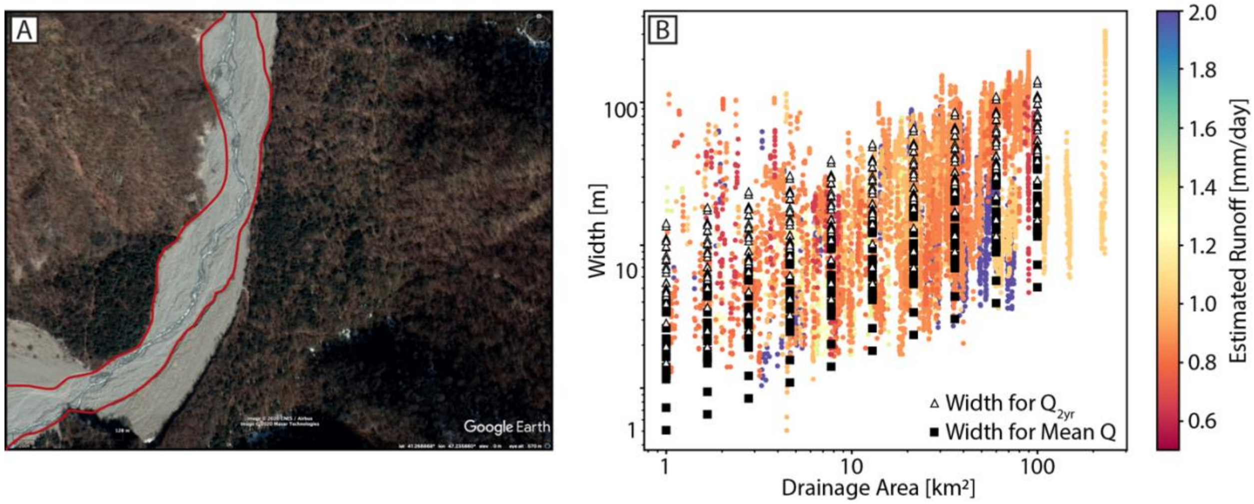

Fig 4. (A) Example of channel width as measured on satellite imagery from Google Earth. (B) Measured widths (dots colored by estimated runoff of each basin) and predicted widths using k_w = 15 and either the mean discharge or the 2-year flood (black symbols) as a function of drainage area. Additional comparisons between width and drainage area scaling are provided in Fig. S10.

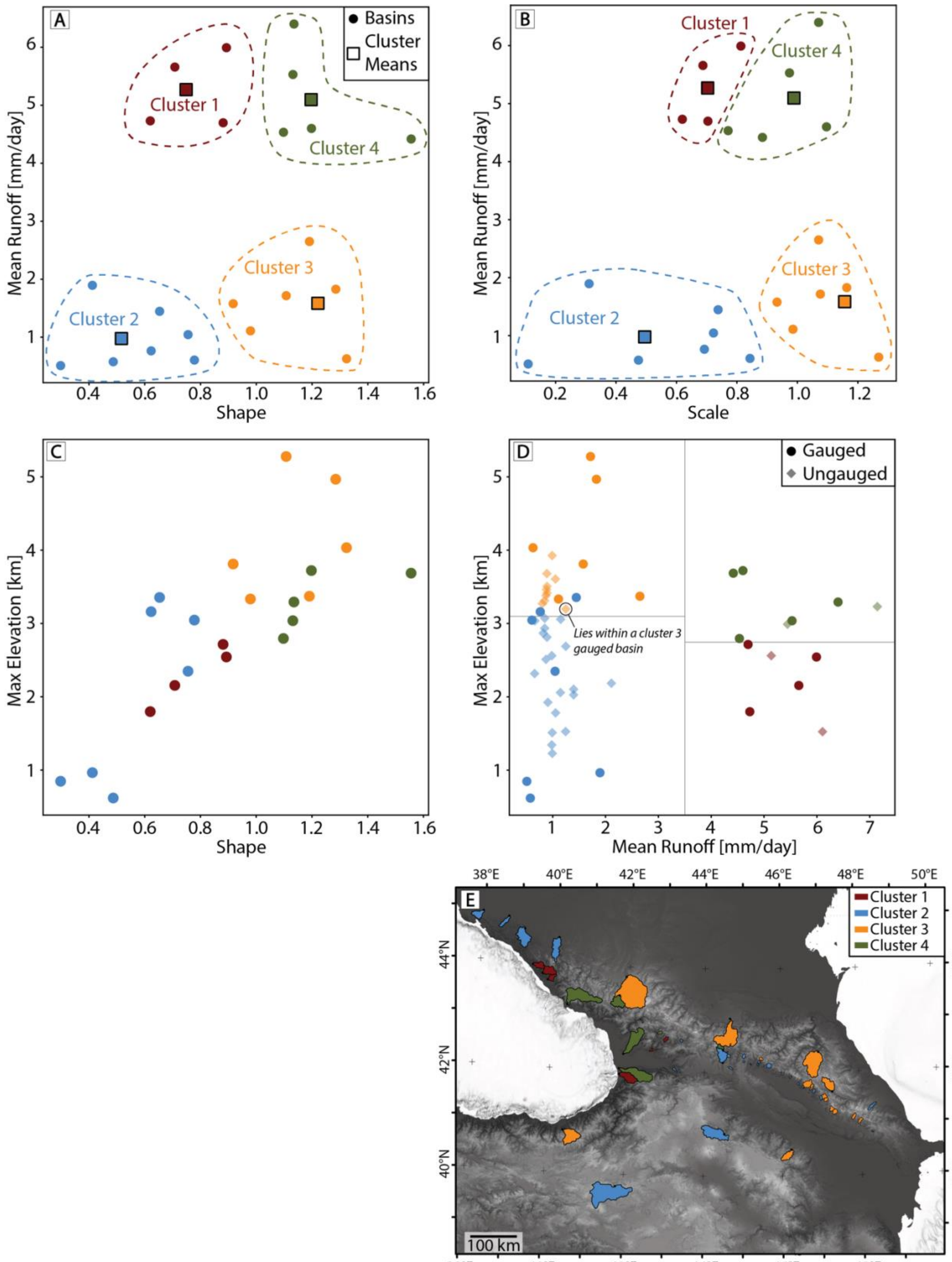

Fig 5. Hydroclimate cluster analysis. (A) Comparison of shape and mean runoff. These two parameters were the input to the k-means cluster analysis. Squares indicate the

single value of shape and mean runoff used for the cluster as a whole in subsequent analysis, see main text. An elbow plot for choosing the number of clusters is provided in Fig. S11. Note that dashed line boundaries are meant aid visualization and do not define known edges of the clusters (B) Comparison of scale and mean runoff, colored by cluster membership. Squares indicate the single value of shape and mean runoff used for the cluster as a whole in subsequent analysis. (C) Comparison of shape and maximum elevation within the catchment for gauged (GRDC) basins. (D) Comparison of mean runoff and maximum elevation for the gauged and ungauged basins. Colors represent cluster membership. For the gauged basins, these are outcomes of the k-means clustering described in the text. For the ungauged basins, they were assigned cluster membership by breaking this space into four quadrants (shown with the light gray lines). For the boundary between cluster 2-3, this was tuned such that a basin which lies within a cluster 3 gauged basin was assigned to cluster 3. (E) Spatial distribution of clusters for both the gauged basins used to define the clusters and ungauged basins assigned to clusters.

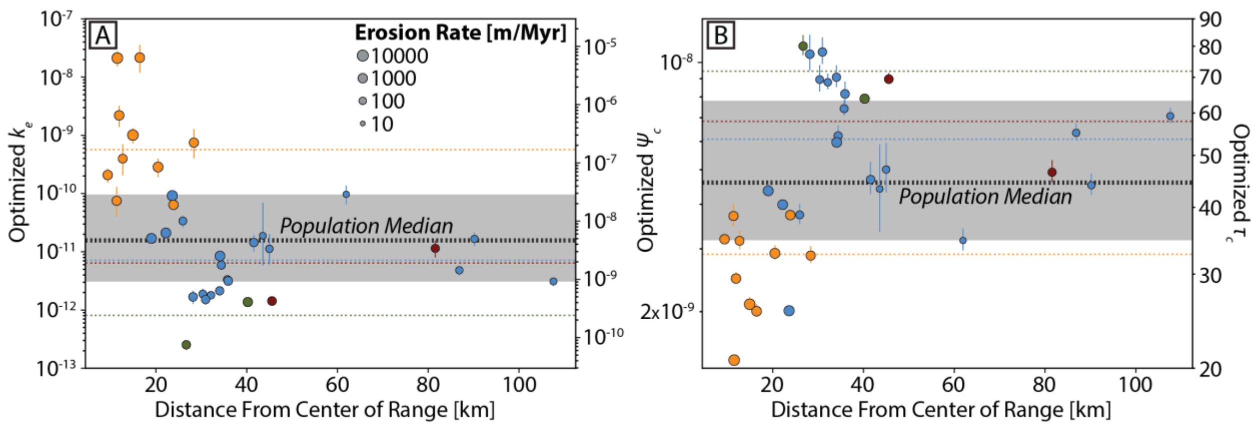

Fig. 6 Results of optimization of k_e (A) and τ_c (B) compared to distance from center of the range (x axis) and erosion rate (scale of dots). Horizontal dotted lines represent median by cluster and for the entire population. Shaded region indicates interquartile range for the whole population estimates. Points are colored by cluster membership (see Fig. 5). Comparison of the optimized values of k_e and τ_c and lithology are presented in Fig. S12.

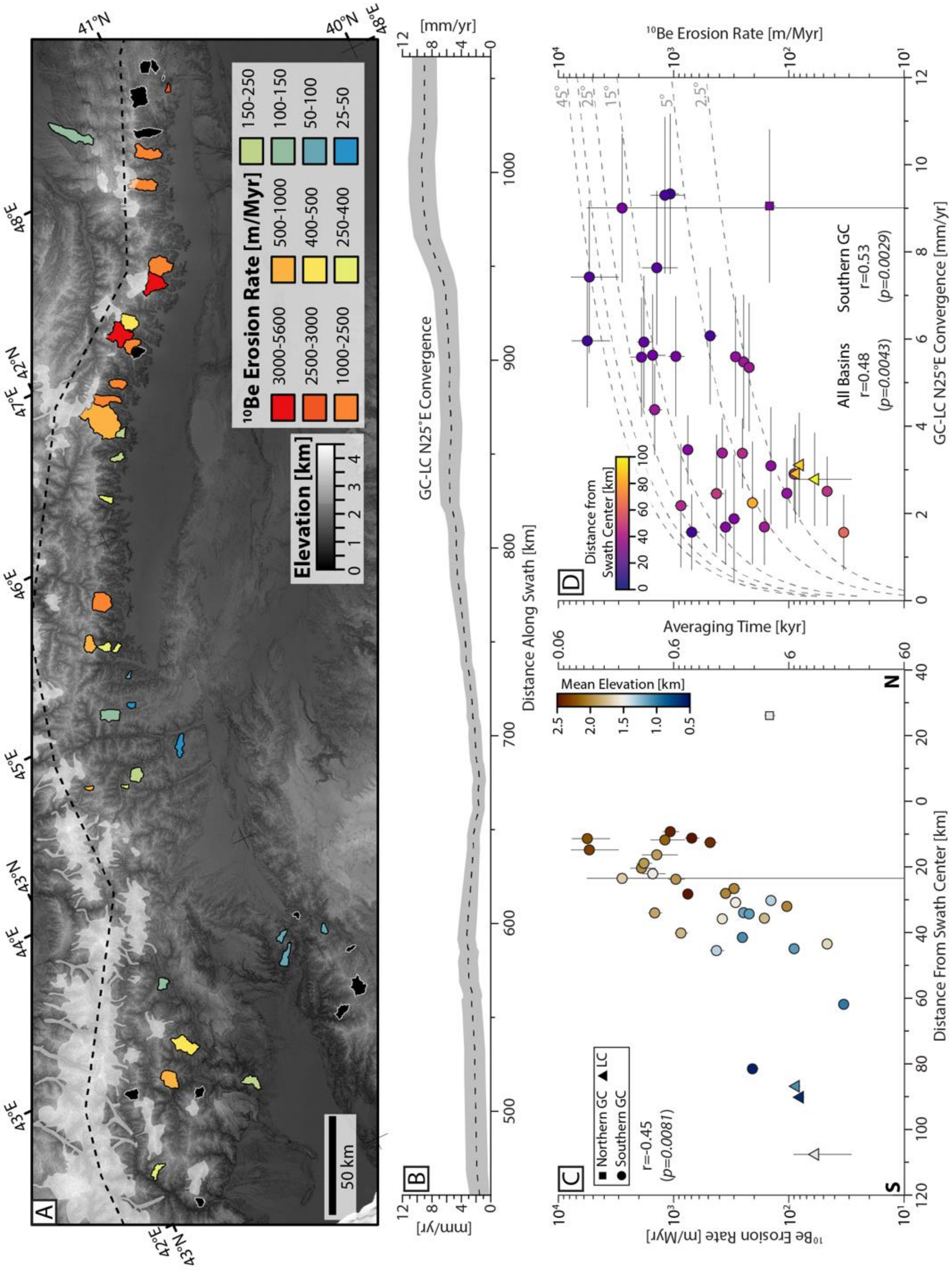

Fig 7. (A) Cosmogenic ^{10}Be erosion rates for sampled basins. Black basins indicate unsuccessful samples (insufficient quartz yield; see Supplemental Methods for additional discussion). White shading represents extent of LGM glaciation (Gobejishvili

et al., 2011) and black dashed line marks center of swath shown in Fig. 1. (B) Estimated N25°E convergence between the GC and LC along the southern margin of the GC, identical to the red curve in Fig 1B. (C) Cosmogenic ^{10}Be erosion rates vs distance from the center of the swath (colored by mean elevation of sampled basins). Pearson's correlation coefficient (r) is shown comparing erosion rates and distance from the swath center, along with respective p value. (D) Cosmogenic ^{10}Be erosion rates vs convergence velocity (7B, colored by distance from the swath center). Contours represent the vertical component of rock uplift if convergence was accommodated along a thrust of a specified dip, these are for reference only and do not imply known structural geometries. Correlation coefficient between E and GC-LC convergence (Fig 1C) is shown. Average time is calculated as the amount of time required to erode 60 cm. A plot of erosion rate as a function of along-strike distance is provided in Fig. S13.

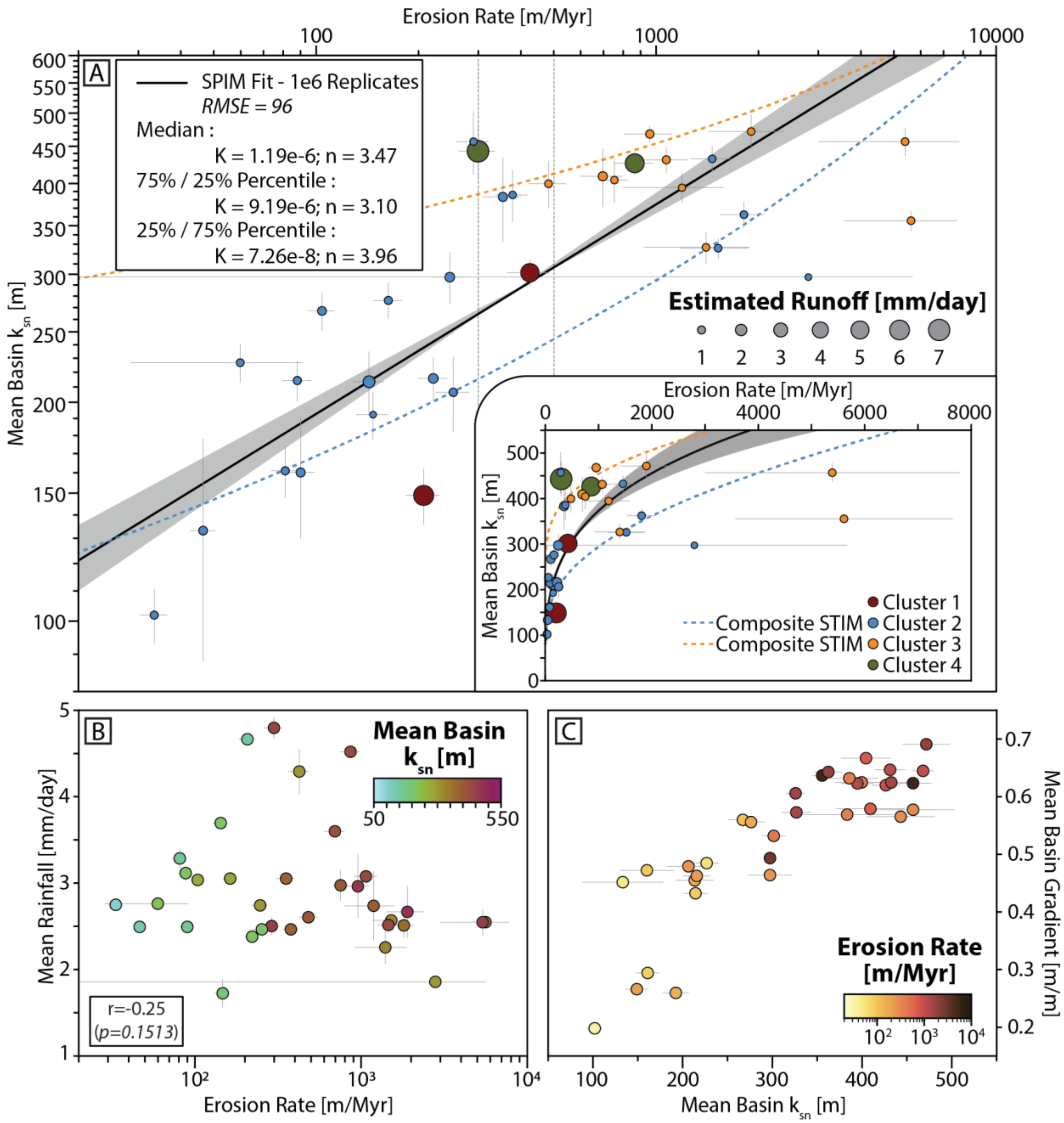

Fig. 8 (A) ^{10}Be erosion rate vs basin-averaged normalized channel steepness (k_{sn}). Individual basins are colored by cluster membership (see Fig. 5D) and the size of the circles are scaled by estimated mean runoff. Curve is the best-fit power law function. Vertical dashed lines highlight the range of E above which k_{sn} becomes largely invariant. Inset shows same data on a linear scale. Details of the power law fit are provided in Fig. S7. Also shown are the composite STIM relationships (Fig. 9) for clusters 2 and 3, which represent the bulk of the data. (B) ^{10}Be erosion rate vs mean rainfall in each basin colored by k_{sn}. Pearson's correlation coefficient (r) between erosion rate and rainfall along with p-value is shown, note that this suggests non-statistically significant correlation between these variables. (C) Mean basin k_{sn}

compared to mean hillslope gradient, colored by *E*. Note that the linear relationship between k_{sn} and gradient reflects that both k_{sn} and gradient become insensitive to increases in erosion rate at ~500 m Myr^{-1} (Fig. S4).

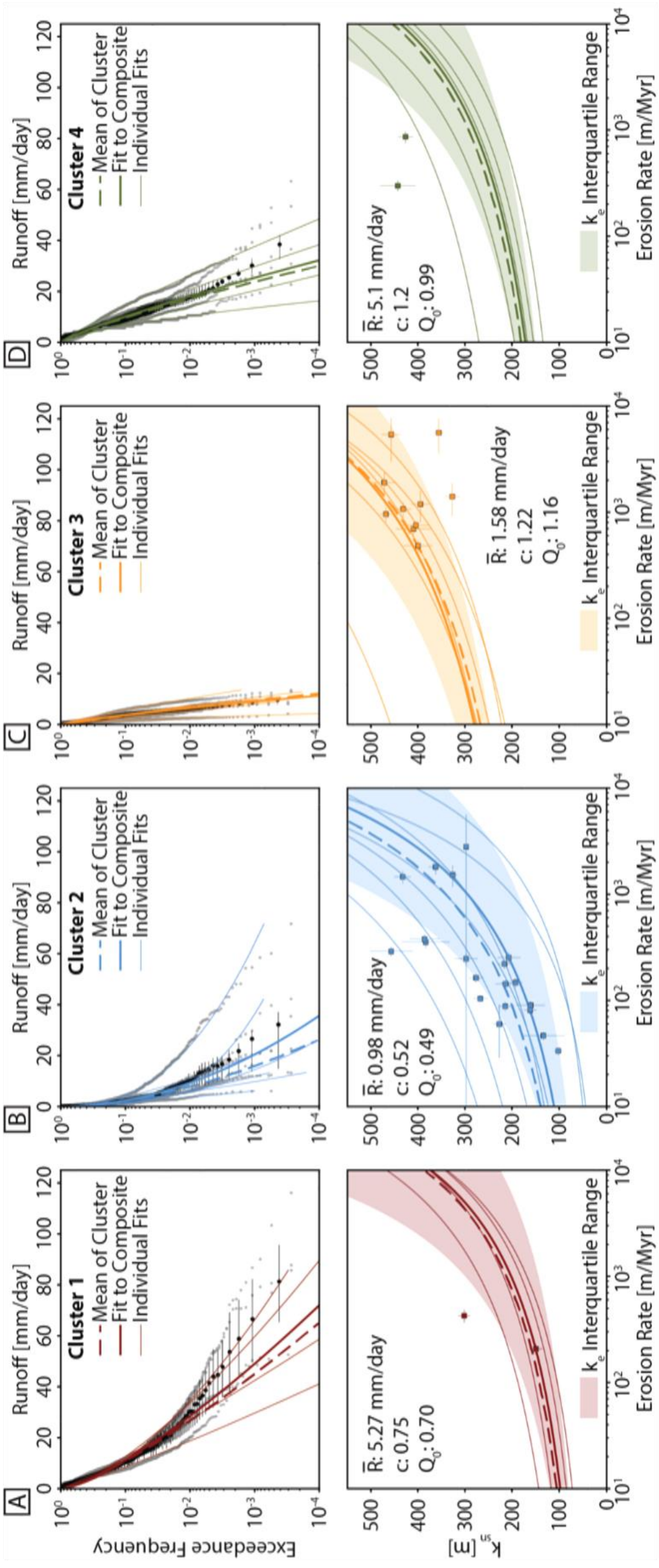

A
B
C
D
Runoff [mm/day]
Exceedance Frequency
Cluster 1
Mean of Cluster
Fit to Composite
Individual Fits
Cluster 2
Mean of Cluster
Fit to Composite
Individual Fits
Cluster 3
Mean of Cluster
Fit to Composite
Individual Fits
Cluster 4
Mean of Cluster
Fit to Composite
Individual Fits
R̄: 5.27 mm/day
c: 0.75
Q0: 0.70
R̄: 0.98 mm/day
c: 0.52
Q0: 0.49
R̄: 1.58 mm/day
c: 1.22
Q0: 1.16
R̄: 5.1 mm/day
c: 1.2
Q0: 0.99
ke Interquartile Range
ksn [m]
Erosion Rate [m/Myr]

Fig. 9 Details of runoff distributions and erosion rates for cluster 1 (A), cluster 2 (B), cluster 3 (C), and cluster 4 (D). For all plots, the top panels display the individual runoff distributions (gray dots) and the fits to those distributions (thin lines). Also displayed are the implied distribution using the mean shape, scale, and runoff from each population (thick dashed lines). Black dots represent binned composite of runoff with interquartile range of runoff within each bin. Thick solid line is the fit to the composite distribution. Bottom panels display implied E-k_{sn} relationships using either the individual mean runoff, shape, and scale parameters for gauged basins (thin lines), using the population mean (thick dashed lines), and using the fit to the composite distribution (thick solid lines). All individual relationships use the median k_e (1.55e-11, e.g., Fig. 6), but shaded region shows range of possible relationships using the interquartile range of k_e and the aggregate distribution values. The mean runoff and composite shape and scale parameters are reported for each cluster.

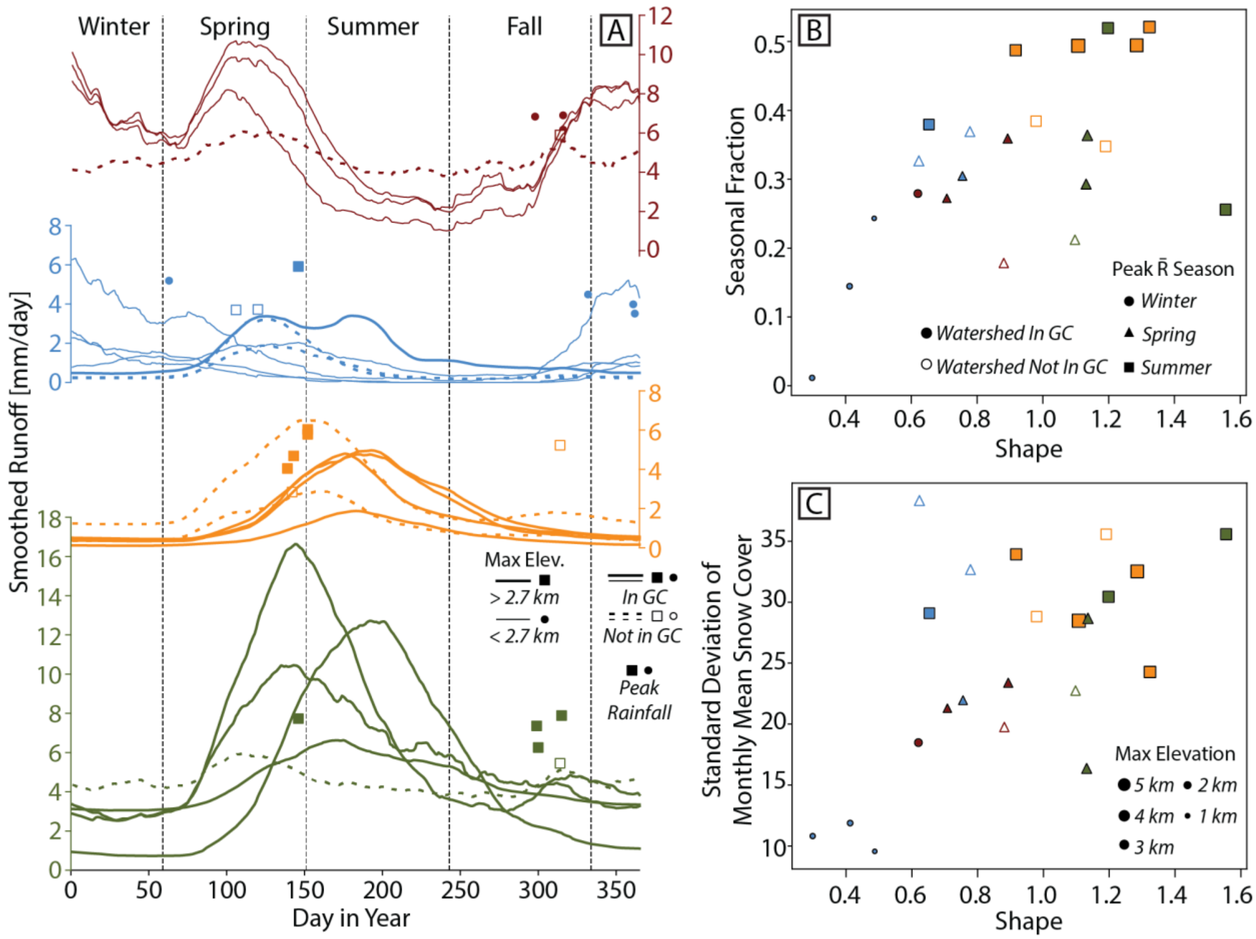

Fig 10. (A) Daily GRDC runoff, averaged over the full length of each dataset and after applying a 31-day moving average. Dots are day of peak rainfall from TRMM processed in the same way for the basin of interest (see Fig. S3 for rainfall time series). Almost all basins show a peak in runoff in either the spring or summer consistent with derivation from snowmelt. (B) Seasonal fraction of runoff versus shape parameter for the distribution. Symbol size is scaled by maximum elevation, shapes indicate the season of

maximum mean runoff, and colors indicate cluster membership. GC basins (solid symbols) show a more consistent relationship than those further afield (open symbols) between seasonal fraction and shape. (C) Standard deviation in mean seasonal snow cover vs shape. Symbols are the same as in 10B. Additional comparisons between fractions and both the shape and scale parameters are provided in Fig. S16.

References

Allen, M.B., Jackson, J., Walker, R., 2004. Late Cenozoic reorganization of the Arabia-Eurasia collision and the comparison of short-term and long-term deformation rates. Tectonics 23, doi:10.1029/2003TC001530-doi:10.1029/2003TC001530.

Anders, A.M., Roe, G.H., Montgomery, D.R., Hallet, B., 2008. Influence of precipitation phase on the form of mountain ranges. Geology 36, 479. https://doi.org/10.1130/G24821A.1

Avdeev, B., Niemi, N.A., 2011. Rapid Pliocene exhumation of the central Greater Caucasus constrained by low-temperature thermochronometry. Tectonics 30. https://doi.org/10.1029/2010TC002808

Balco, G., Stone, J., Lifton, N.A., Dunai, T., 2008. A complete and easily accessible means of calculating surface exposure ages or erosion rates from 10Be and 26Al measurements. Quat. Geochronol. 3, 174–195. https://doi.org/10.1016/j.quageo.2007.12.001

Berghuijs, W.R., Woods, R.A., Hrachowitz, M., 2014. A precipitation shift from snow towards rain leads to a decrease in streamflow. Nat. Clim. Change 4, 583–586. https://doi.org/10.1038/nclimate2246

Berghuijs, W.R., Woods, R.A., Hutton, C.J., Sivapalan, M., 2016. Dominant flood generating mechanisms across the United States: Flood Mechanisms Across the U.S. Geophys. Res. Lett. 43, 4382–4390. https://doi.org/10.1002/2016GL068070

Bierman, P.R., Nichols, K.K., 2004. Rock to sediment - slope to sea with 10Be - rates of landscape change. Annu. Rev. Earth Planet. Sci. 32, 215–235.

Bookhagen, B., Burbank, D., 2006. Topography, relief, and TRMM-derived rainfall variations along the Himalaya. Geophys. Res. Lett. 33, L08405–L08405. https://doi.org/10.1029/2006GL026037

Campforts, B., Vanacker, V., Herman, F., Vanmaercke, M., Schwanghart, W., Tenorio, G.E., Willems, P., Govers, G., 2020. Parameterization of river incision models requires accounting for environmental heterogeneity: insights from the tropical Andes. Earth Surf. Dyn. 8, 447–470. https://doi.org/10.5194/esurf-8-447-2020

Cowgill, E., Forte, A.M., Niemi, N.A., Avdeev, B., Tye, A.R., Trexler, C.C., Javakishvirli, Z., Elashvili, M., Godoladze, T., 2016. Relict basin closure and crustal shortening budgets during continental collision: An example from Caucasus sediment provenance. Tectonics 35, 2918–2947. https://doi.org/10.1002/2016TC004295

Deal, E., Braun, J., Botter, G., 2018. Understanding the Role of Rainfall and Hydrology in Determining Fluvial Erosion Efficiency. J. Geophys. Res. Earth Surf. 123, 744–778. https://doi.org/10.1002/2017JF004393

DiBiase, R.A., Whipple, K.X., 2011. The influence of erosion thresholds and runoff variability on the relationships among topography, climate, and erosion rate. J. Geophys. Res. 116. https://doi.org/10.1029/2011JF002095

DiBiase, R.A., Whipple, K.X., Heimsath, A.M., Ouimet, W.B., 2010. Landscape form and millennial erosion rates in the San Gabriel Mountains, CA. Earth Planet. Sci. Lett. 289, 134–144.

Eckhardt, K., 2008. A comparison of baseflow indices, which were calculated with seven different baseflow separation methods. J. Hydrol. 352, 168–173. https://doi.org/10.1016/j.jhydrol.2008.01.005

Ferrier, K.L., Huppert, K.L., Perron, J.T., 2013. Climatic control of bedrock river incision. Nature 496, 206–209. https://doi.org/10.1038/nature11982

Fisher, G.B., Bookhagen, B., Amos, C.B., 2013. Channel planform geometry and slopes from freely available high-spatial resolution imagery and DEM fusion: Implications for channel width scalings, erosion proxies, and fluvial signatures in tectonically active landscapes. Geomorphology 194, 46–56. https://doi.org/10.1016/j.geomorph.2013.04.011

Forte, A.M., 2021. Lithologic compilation of basins sampled for cosmogenic 10BE in the Greater Caucasus Mountains.

Forte, A.M., Cowgill, E., Murtuzayev, I., Kangarli, T., Stoica, M., 2013. Structural geometries and magnitude of shortening in the eastern Kura fold-thrust belt, Azerbaijan: Implications for the development of the Greater Caucasus Mountains. Tectonics 32. https://doi.org/10.1002/tect.20032

Forte, A.M., Cowgill, E., Whipple, K.X., 2014. Transition from a singly vergent to doubly vergent wedge in a young orogen: The Greater Caucasus. Tectonics 33, 2077–2101. https://doi.org/10.1002/2014TC003651

Forte, A.M., Whipple, K.X., 2019. Short communication : The Topographic Analysis Kit (TAK) for TopoToolbox. Earth Surf. Dyn. 7, 87–95. https://doi.org/10.5194/esurf-7-87-2019

Forte, A.M., Whipple, K.X., Bookhagen, B., Rossi, M.W., 2016. Decoupling of modern shortening rates, climate, and topography in the Caucasus. Earth Planet. Sci. Lett. 449, 282–294. https://doi.org/10.1016/j.epsl.2016.06.013

Forte, A.M., Whipple, K.X., Cowgill, E., 2015. Drainage network reveals patterns and history of active deformation in the eastern Greater Caucasus. Geosphere 11. https://doi.org/10.1130/GES01121.1

Gobejishvili, R., Lomidze, N., Tielidze, L., van der Meer, J.J.M., 2011. Late Pleistocene (Würmian) Glaciations of the Caucasus, in: Ehlers, J., Gibbard, P.L., Hughes, P.D. (Eds.), Quaternary Glaciations - Extent and Chronology. Elsevier, Amsterdam, pp. 141–147.

Harel, M.A., Mudd, S.M., Attal, M., 2016. Global analysis of the stream power law parameters based on worldwide 10Be denudation rates. Geomorphology 268, 184–196. https://doi.org/10.1016/j.geomorph.2016.05.035

Johnson, J.P.L., Whipple, K.X., Sklar, L., 2010. Contrasting bedrock incision rates from snowmelt and flash floods in the Henry Mountains, Utah. Geol. Soc. Am. Bull. 122, 1600–1615.

Kadirov, F., Floyd, M., Alizadeh, A., Guliev, I., Reilinger, R., Kuleli, S., King, R., Toksoz, M.N., 2012. Kinematics of the eastern Caucasus near Baku, Azerbaijan. Nat. Hazards 63, 997–1006.

Kirby, E., Whipple, K.X., 2012. Expression of active tectonics in erosional landscapes. J. Struct. Geol. 44, 54–75.

Kuchment, L.S., Gelfan, A.N., Demidov, V.N., 2010. A spatial model of snowmelt-rainfall runoff formation of the mountain river (by the example of the Upper Kuban River). Russ. Meteorol. Hydrol. 35, 842–850. https://doi.org/10.3103/S1068373910120083

Lague, D., 2014. The stream power river incision model: evidence, theory and beyond. Earth Surf. Process. Landf. 39, 38–61. https://doi.org/10.1002/esp.3462

Lague, D., Hovius, N., Davy, P., 2005. Discharge, discharge variability, and the bedrock channel profile. J. Geophys. Res. 110, F04006–F04006. https://doi.org/10.1029/2004JF000259

Mifsud, C., Fujioka, T., Fink, D., 2013. Extraction and purification of quartz in rock using hot phosphoric acid for in situ cosmogenic exposure dating. Nucl. Instrum. Methods Phys. Res. B 294, 203–207. https://doi.org/10.1016/j.nimb.2012.08.037

Mosar, J., Kangarli, T., Bochud, M., Glasmacher, U.A., Rast, A., Brunet, M.-F., Sosson, M., 2010. Cenozoic-Recent tectonics and uplift in the Greater Caucasus: a perspective from Azerbaijan, in: Sosson, M., Kaymakci, N., Stephenson, R.A., Bergerat, F., Starostenko, V.I. (Eds.), Sedimentary Basin Tectonics from the Black Sea and Caucasus to the Arabian Platform. Geological Society, London, pp. 261–280.

Portenga, E.W., Bierman, P.R., 2011. Understanding Earth’s eroding surface with 10Be. GSA Today 21, 4–10. https://doi.org/10.1130/G111A.1

Reilinger, R., McClusky, S., Vernant, P., Lawrence, S., Ergintav, S., Cakmak, R., Ozener, H., Kadirov, F., Guliev, I., Stepanyan, R., Nadariya, M., Hahubia, G., Mahmoud, S., Sakr, K., ArRajehi, A., Paradissis, D., Al-Aydrus, A., Prilepin, M., Guseva, T., Evren, E., Dmitrotsa, A., Filikov, S.V., Gomez, F., Al-Ghazzi, R., Karam, G., 2006. GPS constraints on continental deformation in the Africa-Arabia-Eurasia continental collision zone and implications for the dynamics of plate interactions. J. Geophys. Res. 111, doi:10.1029/2005JB004051-doi:10.1029/2005JB004051.

Rets, E.P., Dzhamalov, R.G., Kireeva, M.B., Frolova, N.L., Durmanov, I.N., Telegina, A.A., Telegina, E.A., Grigoriev, V.Yu., 2018. RECENT TRENDS Of RIVER RUNOff IN THE NORTH CAUCASUS. Geogr. Environ. Sustain. 11, 61–70. https://doi.org/10.24057/2071-9388-2018-11-3-61-70

Rossi, M.W., Anderson, R.S., Anderson, S.P., Tucker, G.E., 2020. Orographic Controls on Subdaily Rainfall Statistics and Flood Frequency in the Colorado Front Range, USA. Geophys. Res. Lett. 47. https://doi.org/10.1029/2019GL085086

Rossi, M.W., Whipple, K.X., Vivoni, E.R., 2016. Precipitation and evapotranspiration controls on event-scale runoff variability in the contiguous United States and Puerto Rico. J. Geophys. Res. 121. https://doi.org/10.1002/2015JF003446

Schaefli, B., Rinaldo, A., Botter, G., 2013. Analytic probability distributions for snow-dominated streamflow: Snow-Dominated Streamflow Pdfs. Water Resour. Res. 49, 2701–2713. https://doi.org/10.1002/wrcr.20234

Scherler, D., Bookhagen, B., Strecker, M.R., 2014. Tectonic control on 10 Be-derived erosion rates in the Garhwal. J. Geophys. Res. Earth Surf. 119, 83–105. https://doi.org/10.1002/2013JF002955

Scherler, D., DiBiase, R.A., Fisher, G.B., Avouac, J.-P., 2017. Testing monsoonal controls on bedrock river incision in the Himalaya and Eastern Tibet with a stochastic-threshold stream power model. J. Geophys. Res. Earth Surf. 122, 1389–1429. https://doi.org/10.1002/2016JF004011

Schwanghart, W., Scherler, D., 2014. Short Communication: TopoToolbox 2 - MATLAB based software for topographic analysis and modeling in Earth surface sciences. Earth Surf. Dyn. 2, 1–7. https://doi.org/10.5194/esurf-2-1-2014

Shobe, C.M., Tucker, G.E., Rossi, M.W., 2018. Variable-Threshold Behavior in Rivers Arising From Hillslope-Derived Blocks. J. Geophys. Res. Earth Surf. 123, 1931–1957. https://doi.org/10.1029/2017JF004575

Sloto, R.A., Crouse, M.Y., 1996. HYSEP: A Computer Program for Streamflow Hydrograph Separation and Analysis. https://doi.org/10.3133/wri964040

Sokhadze, G., Floyd, M., Godoladze, T., King, R., Cowgill, E.S., Javakhishvili, Z., Hahubia, G., Reilinger, R., 2018. Active convergence between the Lesser and Greater Caucasus in Georgia: Constraints on the tectonic evolution of the Lesser–Greater Caucasus continental collision. Earth Planet. Sci. Lett. 481, 154–161. https://doi.org/10.1016/j.epsl.2017.10.007

Stone, J.O., 2000. Air pressure and cosmogenic isotope production. J. Geophys. Res. Solid Earth 105, 23753–23759. https://doi.org/10.1029/2000JB900181

Sutcliffe, J.V., Farquharson, F.A.K., Tate, E.L., Folwell, S.S., 2008. Flood regimes in the Southern Caucasus: the influence of precipitation on mean annual floods and frequency curves. Hydrol. Res. 39, 385–401. https://doi.org/10.2166/nh.2008.025

Trexler, C.C., Cowgill, E., Spencer, J.Q.G., Godoladze, T., 2020. Rate of active shortening across the southern thrust front of the Greater Caucasus in western Georgia from kinematic modeling of folded river terraces above a listric thrust. Earth Planet. Sci. Lett. 544, 116362. https://doi.org/10.1016/j.epsl.2020.116362

Tucker, G.E., 2004. Drainage basin sensitivity to tectonic and climatic forcing: Implications of a stochastic model for the role of entrainment and erosion thresholds. Earth Surf. Process. Landf. 29, 185–204. https://doi.org/10.1002/esp.1020

Vasil’chuk, Yu.K., Rets, E.P., Chizhova, Ju.N., Tokarev, I.V., Frolova, N.L., Budantseva, N.A., Kireeva, M.B., Loshakova, N.A., 2016. Hydrograph separation of the Dzhankuat River, North Caucasus, with the use of isotope methods. Water Resour. 43, 847–861. https://doi.org/10.1134/S0097807816060087

Verdiev, R.G., 2009. Computation and prediction of the flood runoff of the Eastern Caucasus Rivers. Russ. Meteorol. Hydrol. 34, 46–50.

Vezzoli, G., Garzanti, E., Limonta, M., Radeff, G., 2020. Focused erosion at the core of the Greater Caucasus: Sediment generation and dispersal from Mt. Elbrus to the Caspian Sea. Earth-Sci. Rev. 200, 102987. https://doi.org/10.1016/j.earscirev.2019.102987

Vezzoli, G., Garzanti, E., Vincent, S.J., Ando, S., Carter, A., Resentini, A., 2014. Tracking sediment provenance and erosional evolution of the western Greater Caucasus. Earth Surf. Process. Landf. https://doi.org/10.1002/esp.3567

Vincent, S.J., Carter, A., Lavrishchev, A., Rice, S.P., Barabadze, T.G., Hovius, N., 2011. The exhumation of the western Greater Caucasus: a thermochronometric study. Geol. Mag. 148, 1–21. https://doi.org/10.1017/S0016756810000257

Vincent, S.J., Somin, M.L., Carter, A., Vezzoli, G., Fox, M., Vautravers, B., 2020. Testing Models of Cenozoic Exhumation in the Western Greater Caucasus. Tectonics 39. https://doi.org/10.1029/2018TC005451

Whipple, K.X., 2009. The influence of climate on the tectonic evolution of mountain belts. Nat. Geosci. 2, 97–104.

Whipple, K.X., Meade, B., 2004. Controls on the strength of coupling among climate, erosion, and deformation in two-sided, frictional orogenic wedges at steady state. J. Geophys. Res. 109, F01011–F01011. https://doi.org/10.1029/2003JF000019
Willett, S.D., 1999. Orogeny and orography: The effects of erosion on the structure of mountain belts. J. Geophys. Res. 104, 28,928-957,981.
Wilson, P.S., Toumi, R., 2005. A fundamental probability distribution for heavy rainfall. Geophys. Res. Lett. 32, n/a-n/a. https://doi.org/10.1029/2005GL022465
Wulf, H., Bookhagen, B., Scherler, D., 2016. Differentiating between rain, snow, and glacier contributions to river discharge in the western Himalaya using remote-sensing data and distributed hydrologic modeling. Adv. Water Resour. 88, 152–169. https://doi.org/10.1016/j.advwatres.2015.12.004